The Astrophysical Journal, 725:1421–1428, 2010 December 20 doi:10.1088/0004-637X/725/2/1421

TRANSPORT OF THE FIRST ROCKS OF THE SOLAR SYSTEM BY X-WINDS

Renyu Hu
Department of Earth, Atmospheric and Planetary Sciences, Massachusetts Institute of Technology, Cambridge, MA 02139, USA; hury@mit.edu
Received 2010 February 28; accepted 2010 October 12; published 2010 November 29

ABSTRACT

It has been suggested that chondrules and calcium–aluminum-rich inclusions (CAIs) were formed at the inner edge of the protoplanetary disk and then entrained in magnetocentrifugal X-winds. We study trajectories of such solid bodies with the consideration of the central star gravity, the protoplanetary disk gravity, and the gas drag of the wind. The efficiency of the gas drag depends on a parameter η, which is the product of the solid body size and density. We find that the gravity of the protoplanetary disk has a non-negligible effect on the trajectories. If a solid body re-enters the flared disk, the re-entering radius depends on the stellar magnetic dipole moment, the disk's gravity, the parameter η, and the initial launching angle. The disk's gravity can make the re-entering radius lower by up to 30%. We find a threshold η, denoted as η_t, for any particular configuration of the X-wind, below which the solid bodies will be expelled from the planetary system. η_t sensitively depends on the initial launching angle, and also depends on the mass of the disk. Only the solid bodies with an η larger than but very close to η_t can be launched to a re-entering radius larger than 1 AU. This size-sorting effect may explain why chondrules come with a narrow range of sizes within each chondritic class. In general, the size distributions of CAIs and chondrules in chondrites can be determined from the initial size distribution as well as the distribution over the initial launching angle.

Key words: celestial mechanics – comets: general – meteorites, meteors, meteoroids – minor planets, asteroids: general – protoplanetary disks – stars: protostars

1. INTRODUCTION

X-winds are high-speed bipolar-collimated jets around young stellar objects (YSOs) powered by enhanced magnetic activities and disk–magnetosphere interactions (Shu et al. 1996, 1997). An X-wind can be driven magnetocentrifugally from the inner edge of the disk where accreting gas is either diverted onto stellar field lines to flow onto the star or to be flung outward with the wind (Shu et al. 1994a, 1994b).

X-winds are also suggested to be the underlying mechanism for the production of calcium–aluminum-rich inclusions (CAIs) and chondrules for our solar system (Shu et al. 2001). The subsolar reconnection ring (X-region) at the inner edge of the protoplanetary disk provides high-temperature environment to form CAIs and chondrules, and the X-winds can lift the processed rocks back to colder regions of the disk. At least 50% by mass of all the magnesium–iron silicates that finally constructed planetesimals and planets may have been processed as chondrules or CAIs (Tayler 1992; Shu et al. 1996).

Isotopic measurements also provide evidence of the X-wind origin of planetary materials. CAIs have $^{18}O/^{16}O$ and $^{17}O/^{16}O$ ratios that are several percent lower than any other meteoritic and planetary materials in the solar system (Clayton 1993). This isotopic feature can be explained by photochemical self-shielding of carbon monoxide in the solar nebula, which requires that planetary materials passed through the inner part of the accreting protoplanetary disk (Clayton 2002). Again the processed materials need to be returned back to colder regions by X-winds.

However, there are also other formation mechanisms that have been proposed to explain the chemical, mineral, and isotopical properties of chondrules, such as exothermic chemical reactions, nebular lightning, magnetic reconnection flares, gas dynamic shock waves in the protoplanetary nebula, radiative heating, etc. (see Rubin 2000 for an extensive review). Desch et al. (2010) not only critically examine the X-wind model for the formation of chondrules and CAIs against isotopical and mineralogical evidences, but also advocate detail modeling on the fate of the particles launched by the outflow to see if the particles can be retained in proper annuli of the disk.

The parent bodies of chondritic meteorites originate mostly from the asteroid belt (AB) at about 2.5 astronomical units (AU) from the Sun. Recent observations find evidence of CAI-type and chondrule-like particles present in a short-term comet 81P/Wild 2 (Swindle & Campins 2004; Brownlee et al. 2006; Flynn et al. 2006; Nakamura et al. 2008). Wooden (2008) concluded from mineralogy investigations that these refractory grains should be pre-accretionary with respect to the formation of asteroids and efficient outward radial transport mechanism is required. This discovery requires large-scale radial transport mechanisms, such as X-winds and the turbulent diffusion of particles (e.g., Ciesla 2009). However, it has not been studied whether X-winds are able to drive solid bodies to the radius of the Kuiper Belt (KB), or >30 AU.

It has not yet been clearly explained under what conditions an X-wind can deliver chondrules and CAIs to the AB or the KB. Shu et al. (1996) and Shang (1998) provide several trajectories of solid bodies in X-winds in the dimensionless form without the consideration of protoplanetary disk gravity or the vertical geometry of the disk. Liffman (2005) investigated the size-sorting effect of chondrules from magnetic-pressure-driven jet flows, but only for distance $\leqslant 3$ AU from the Sun. In this paper, we study the transport of solid bodies (e.g., CAIs and chondrules) by X-winds, with the protoplanetary disk's gravity and vertical geometry taken into account. We also investigate whether and where the launched solid bodies re-enter the disk and how the re-entering radius depends on the stellar magnetic dipole moment and the size and density of the solid bodies.

Table 1
Definition and X-wind Properties of All States Considered in This Paper

States[a]	M_* ($M_\odot$)	$\dot{M}_D$ ($M_\odot$ yr^{-1})	μ_* (G cm^{-3})	R_X (cm)	Ω_X (s^{-1})	$\bar{v}_w$ (cm s^{-1})	T_{peak}[b] (K)
EH	0.5	2×10^{-6}	6	1.43×10^{12}	4.76×10^{-6}	1.43×10^{7}	1325
EA	0.5	2×10^{-6}	2	7.64×10^{11}	1.22×10^{-5}	1.96×10^{7}	1837
EL	0.5	2×10^{-6}	1	5.14×10^{11}	2.21×10^{-5}	2.39×10^{7}	2270
RH	0.8	1×10^{-7}	3	2.12×10^{12}	3.34×10^{-6}	1.49×10^{7}	941
RA	0.8	1×10^{-7}	1	1.13×10^{12}	8.57×10^{-6}	2.04×10^{7}	1299
RL	0.8	1×10^{-7}	0.5	7.61×10^{11}	1.55×10^{-5}	2.48×10^{7}	1598

Notes. Each state is defined by a set of parameters (M_*, $\dot{M}_D$, μ_*). For each case, key X-wind properties R_X, Ω_X, $\bar{v}_w$, and T_{peak} are calculated based on Equations (1)–(4). Full names of cases are given following the table, but simplified names, given in the first column of the table, are used in the text.

[a] EH: embedded stage, high state; EA: embedded stage, average state; EL: embedded stage, low state; RH: revealed stage, high state; RA: revealed stage, average state; RL: revealed stage, low state.

[b] For EH, EA, and EL cases, $L_* = 4.4\,L_\odot$ and $R_* = 3\,R_\odot$ are used in the calculation of T_{peak}, where $L_\odot$ and $R_\odot$ are the current luminosity and radius of the Sun. Similarly, for RH, RA, and RL cases, we assume $L_* = 2.5\,L_\odot$ and $R_* = 3\,R_\odot$.

2. MODEL

2.1. X-wind Configurations

In this section, we provide an introduction on the X-wind configurations based on Shu et al. (1994a, 1996) and identify several stellar and disk parameters that govern the X-wind.

An accreting protoplanetary disk that interacts with the rotating magnetosphere of a protostar with a pure dipole is truncated at a radius of

$$R_X = C_1 \left(\frac{\mu_*^4}{G M_* \dot{M}_D^2} \right)^{1/7}, \quad (1)$$

where μ_* is the stellar dipole moment, M_* is the stellar mass, $\dot{M}_D$ is the inflow rate of the disk, G is the gravitational constant, and C_1 is a dimensionless coefficient that we assume to be unity in the following (e.g., Shu et al. 1996). In steady state, the inner disk edge corotates with the star at the Keplerian angular velocity of

$$\Omega_* = \Omega_X = \left(\frac{G M_*}{R_X^3} \right)^{1/2}. \quad (2)$$

The wind has a terminal velocity $\bar{v}_w$ when leaving the X region. The terminal velocity can be written as

$$\bar{v}_w = (2 J_g - 3)^{1/3} R_X \Omega_X, \quad (3)$$

where J_g is the dimensionless specific angular momentum of the gas (Shu et al. 1994a).

The formation of CAIs requires the thermal treatment at 1800–2200 K. CAIs and chondrules entrained in the X-wind experience the peak temperature when they are lifted into direct sunlight. The peak temperature is given by Shu et al. (1996) as

$$T_{peak} = \left\{ \frac{L_*}{16\pi\sigma R_X^2} + \frac{L_*}{8\pi^2\sigma R_*^2} \left[\arcsin\left(\frac{R_*}{R_X} \right) - \left(\frac{R_*}{R_X} \right) \left(1 - \frac{R_*^2}{R_X^2} \right)^{1/2} \right] \right\}^{1/4}, \quad (4)$$

where L_* is the stellar luminosity, σ is the Stefan–Boltzmann constant, and R_* is the radius of the star.

From above, we see that the physical properties of X-winds are determined by three parameters of a planetary system: M_*, μ_*, and $\dot{M}_D$. In theory, the X-wind can exist in either the "embedded" stage, when the protostar is still embedded in its natal envelope of gas and dust, or the "revealed" stage, when the outflowing wind has reversed the infall of the envelope and revealed the central star and the accretion disk (Shu et al. 1996). At different stages, the star has different masses, the stellar magnetic dipole moment varies in different ranges, and the accretion rate has different values. As long as the lifetime of these two stages is constrained fairly well by the observations of YSOs, we use typical values of M_* and $\dot{M}_D$ for each stages, and let μ_* vary in different ranges, respectively. Following Shu et al. (1997), we define a high state, an average state, and a low state according to the value of μ_* for each stage, as shown in Table 1. Key X-wind properties R_X, Ω_X, $\bar{v}_w$, and T_{peak} of each state are also given in Table 1. As evident from Table 1, a proto-Sun with a stronger magnetic field truncates the protoplanetary disk at a larger radius, and therefore has lower T_{peak} and $\bar{v}_w$. Notably, CAIs can only form during the EA and EL cases.

For each state, the gas density and flow velocity of the X-wind can be determined numerically, from a set of equations involving the conservation of mass, specific momentum, and specific energy (see Shang 1998 for the detail formulation). In the following, we formulate the equation of motion in the inertial frame, with the cylindrical coordinates (l, ϕ, z) centered at the star and with $z = 0$ defining the midplane of the disk. The asymptotic behavior of the X-wind dynamics sufficiently far from the X-region (i.e., $l > 50 R_X$) is (1) the poloidal velocity reaches the terminal velocity, (2) the toroidal velocity decreases as l^{-1}, and (3) the density of the wind falls off as l^{-2}. Assuming the streamlines to be straight lines originating from the X-region and the open angle of the bipolar wind to be $\theta_w = 45°$, we follow the procedure of Shang (1998) to construct the X-wind as the background for the motion of the solid body.

2.2. Extended Model

In this section, we set up the framework to calculate the trajectories of solid bodies entrained in the X-wind. A solid body with size R_s and density ρ_s entrained in an X-wind is subject to three forces: the gravity of the star, the gravity of the protoplanetary disk, and the aerodynamic drag of the X-wind. The total force exerted on the solid body is

$$\mathbf{F} = -\frac{G M_* m_s}{r^3} \mathbf{r} - A(l, z) m_s \mathbf{e}_z - B(l, z) m_s \mathbf{e}_l + \mathbf{F}_{drag}, \quad (5)$$

where m_s is the mass of the solid body and r is the distance from the solid body to the center of star. The second and the third terms on the right-hand side of Equation (5) represent the protoplanetary disk gravity, which has not been included in previous trajectory calculations. $A(l, z)$ and $B(l, z)$ can be calculated by the superposition of gravitational contributions from surface elements throughout the disk, namely,

$$A(l, z) = -\frac{\partial}{\partial z}\int_{R_{\rm in}}^{R_{\rm out}}\int_0^{\pi}\frac{2G\Sigma(l')l'd\phi'dl'}{\sqrt{l'^2 + l^2 + z^2 - 2l'l\cos\phi'}}, \quad (6)$$

$$B(l, z) = -\frac{\partial}{\partial l}\int_{R_{\rm in}}^{R_{\rm out}}\int_0^{\pi}\frac{2G\Sigma(l')l'd\phi'dl'}{\sqrt{l'^2 + l^2 + z^2 - 2l'l\cos\phi'}}, \quad (7)$$

where l' and ϕ' are dummy variables of integration spanning the whole disk, $R_{\rm in}$ and $R_{\rm out}$ are the inner and outer edges of the protoplanetary disk, and $\Sigma(l)$ is the surface density of the disk. In the calculation of the disk's gravity, we assume the geometry of the disk to be a thin plane at $z = 0$, and use $R_{\rm in} = R_{\rm X}$ and $R_{\rm out} = 40$ AU. The integrals can be evaluated numerically once we know the surface density profile of the protoplanetary disk.

We adopt that the disk has the mass distribution as the standard minimum mass solar nebula (MMSN) given by Hayashi (1981). However, the density of the protoplanetary disk might be much higher. For example, Desch (2007) estimated a denser MMSN based on the NICE model. The disk's surface density in our model is parameterized as

$$\Sigma(l) = f \times 1700\left(\frac{l}{1\ {\rm AU}}\right)^{-3/2}\ {\rm g\ cm^{-2}}, \quad (8)$$

where f is a multiplying factor specifying the mass of the disk and the rest is the MMSN profile given by Hayashi (1981). Note that Desch (2007) suggested the surface density exponent to be -2.2 instead of -1.5, but in this work we adopt the profile by Hayashi (1981). The acceleration due to the disk gravity $A(l, z)$ and $B(l, z)$ can then be computed numerically.

The protoplanetary disk has the vertical extension that may intercept the solid body trajectory and influence the radius where the solid body re-enters the disk. Assuming that the disk is supported by thermal pressure, the scale height of the disk is

$$H(l) = \sqrt{\frac{2k_{\rm B}T(l)l^3}{GM_*\mu M_{\rm H}}}, \quad (9)$$

where $k_{\rm B}$ is the Boltzmann constant, μ is the mean molecular mass in the atomic mass unit (for the solar abundance $\mu = 2.3$), $M_{\rm H}$ is the mass of hydrogen atom, and $T(l)$ is assumed to be the temperature of the MMSN disk as $T(l) = 280\ l^{-1/2}$ K (see Hartmann 2009). In the following, we regard the scale height in Equation (9) as the "boundary" of the disk. Once the vertical position of the solid body becomes smaller than the scale height of the disk, $z < H$, the solid body re-enters the disk, and then the trajectory calculation is terminated. We do not intend to follow the trajectories of the solid bodies inside the disk. Once the horizontal position of the solid body becomes outside the disk, or $l > 40$ AU, the solid body is ejected from the planetary system. In this work, we assume a thin disk when calculating the gravitational force from the disk. Still, we do consider the vertical geometry of the disk using a realistic "flared disk" model when determining the radius where the solids re-enter the disk. We will demonstrate that the vertical structure of the disk has a significant effect on the re-entering radius.

The Epstein gas drag applies when the relative velocity of the solid body and the wind are less than the sound speed of the wind, and the radius of the solid body is smaller than the mean free path of the gas. For example, the mean free path of the wind is 10–10^2 cm during the embedded stage, and 10^2–10^3 cm during the revealed stage. Therefore, when calculating the trajectories of chondrule- or CAI-size solid bodies entrained in X-winds, the Epstein gas drag law should be used, namely,

$$\mathbf{F}_{\rm drag} = \frac{4}{3}\pi R_s^2\rho_w\left[(\mathbf{v}_w - \mathbf{v}_s)^2 + c_w^2\right]^{1/2}(\mathbf{v}_w - \mathbf{v}_s), \quad (10)$$

where ρ_w, c_w, and $\mathbf{v}_w$ are the density, sound speed, and bulk velocity of the wind, respectively, and $\mathbf{v}_s$ is the velocity of the solid body (Weidenschilling 1977; Shang 1998; Youdin & Chiang 2004). The gas drag depends on the density and velocity of the wind. The acceleration due to the gas drag is

$$\mathbf{a}_{\rm drag} \equiv \frac{\mathbf{F}_{\rm drag}}{m_s} = \frac{\rho_w}{\eta}\left[(\mathbf{v}_w - \mathbf{v}_s)^2 + c_w^2\right]^{1/2}(\mathbf{v}_w - \mathbf{v}_s), \quad (11)$$

where we define the drag efficiency parameter $\eta \equiv R_s\rho_s$. The gas drag is more effective for a solid body with smaller η, meaning smaller or less dense.

Assuming that a solid body is launched at the initial angle of θ_0 with respect to the midplane of the disk from the reconnection ring at the speed of the local X-wind, we integrate the equations of motion (Equation (5)) numerically to find the trajectory of the solid body. The allowing range of θ_0 is $[0,\ \theta_w]$. In summary, the model calls six parameters: three parameters to specify the X-wind, M_*, $\dot{M}_{\rm D}$, and μ_*; f to specify the mass of the protoplanetary disk; η to specify the efficiency of the gas drag; and θ_0 to specify the initial launching angle of the solid body. For any particular state in Table 1, the former three wind-related parameters are fixed, and the latter three parameters are free to be explored.

3. RESULTS

3.1. Trajectories of Solid Bodies

The trajectories of solid bodies of different size and density (or η) in the EA and RA states are plotted in Figure 1. Here, we assume $f = 5$ and only explore the situations of maximum lift ($\theta_0 = \theta_w$) and intermediate lift ($\theta_0 = \theta_w/2$). It is evident from Figure 1 that smaller and less dense objects can be launched to a larger orbit, in agreement with previous works (e.g., Shu et al. 1996). Note that although the left and the right panels of Figure 1 appear to be very similar, they show trajectories of solid bodies with very different η (see the caption for details). Based on Figure 1, the X-wind in the EA state can lift much larger and denser (or larger η) solid bodies to a significantly larger radius than that in the RA state does.

The vertical extent of the disk intercepts some trajectories. From Figure 1, the trajectories approach straight lines in the l–z plot at large l and z, in agreement with previous works of Shu et al. (1996), Shang (1998), and Liffman (2005). Without the consideration of disk's flared vertical geometry, these straight-line trajectories may easily be interpreted as "ejection." For example, in the EA case, $f = 5$ and $\theta_0 = \theta_w$, the solid body with $\eta = 1.3$ cgs units re-enters the disk at $l = 8.5$ AU (see the left panel of Figure 1). If the disk was assumed to be a thin surface, such an object would be ejected from the system.

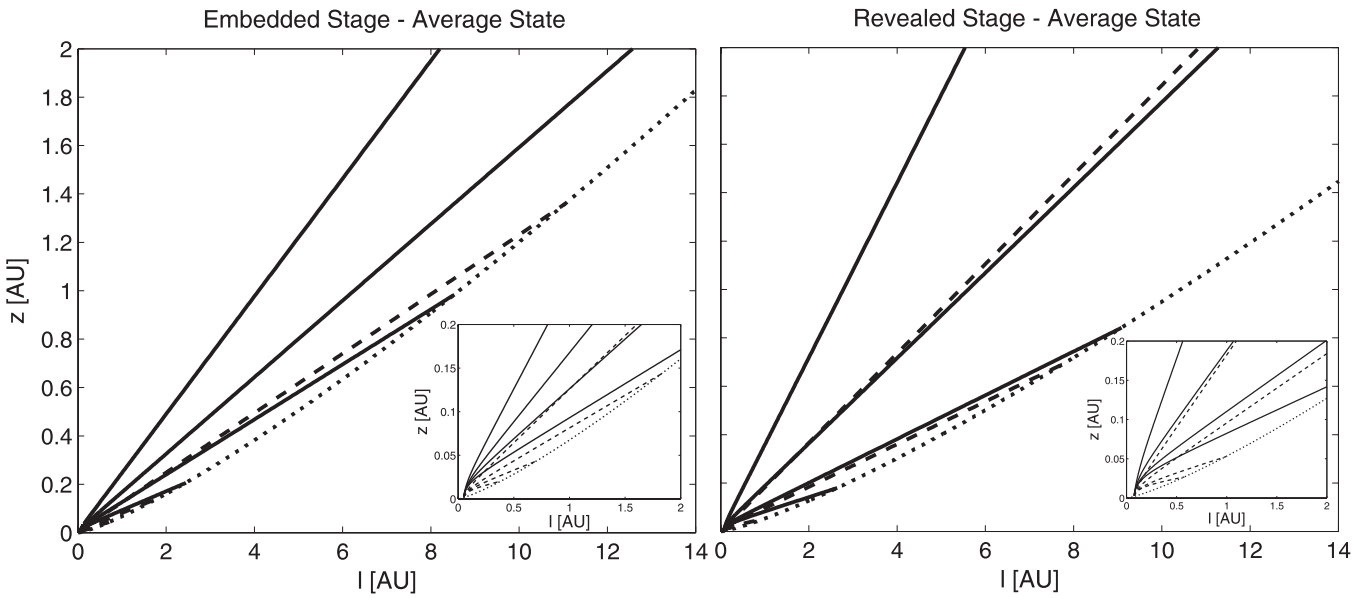

Figure 1. Trajectories of solid bodies entrained in X-winds of the EA (left) and RA states (right) with $f = 5$. In both panels, the solid lines are the trajectories of the maximum initial launching angle ($\theta_0 = \theta_w$), and the dashed lines are the trajectories of the intermediate initial launching angle ($\theta_0 = \theta_w/2$). The dotted lines show the scale height of the disk. Both panels have the same vertical axis, so the tags are only shown in the left panel. In the bottom right region of each panel is the enlarged figure showing the details of the trajectories in $l < 2$ AU. Left: from top to bottom the solid lines (or dashed lines) correspond to trajectories of $\eta \sim 0.6$, 1.0, 1.3, and 1.6 cgs units, respectively. Note that for $\theta_0 = \theta_w$, the solid bodies of $\eta \sim 0.6$ and 1.0 cgs units are expelled from the planetary system; and for $\theta_0 = \theta_w/2$, none of these solid bodies is expelled from the planetary system. Right: from top to bottom the solid lines (or dashed lines) correspond to trajectories of $\eta \sim 0.01$, 0.03, 0.05, and 0.06 cgs units, respectively. Note that for $\theta_0 = \theta_w$, the solid bodies of $\eta \sim 0.01$ and 0.03 cgs units are expelled from the planetary system; and for $\theta_0 = \theta_w/2$, only the solid body of $\eta \sim 0.01$ cgs units is expelled from the planetary system.

Therefore, one has to consider the disk's vertical geometry in order to yield realistic diagnostics on whether the solid bodies re-enter the disk or at what radius the solid bodies re-enter the disk.

The initial launching angle θ_0 has a large effect on the trajectories of the solid bodies. From Figure 1, a solid body is launched to a much larger orbit when $\theta_0 = \theta_w$. For example, in the EA case and $f = 5$, a solid body with $\eta = 1$ cgs unit is ejected from the system if $\theta_0 = \theta_w$, but re-enters the disk at $\sim$2 AU if $\theta_0 = \theta_w/2$ (see Figure 1). For another example, in the EA case and $f = 5$, a solid body with $\eta = 1.3$ cgs unit re-enters the disk at $\sim$8.5 AU if $\theta_0 = \theta_w$, but re-enters the disk at much smaller radius ($\sim$0.7 AU) if $\theta_0 = \theta_w/2$. Therefore, if numbers of solid bodies of such η are initially launched from various angles in $[0,\ \theta_w]$, the X-wind spreads them to the disk's various annuli up to $\sim$8.5 AU. In general, under the same condition, a solid body can be lifted to a larger orbit and thus re-enters the disk at a larger radius if initially launched from a larger angle.

There exists a threshold value of η of solid bodies for any particular X-wind configuration, disk's mass and initial launching angle, denoted as η_t, below which the solid bodies will be expelled from the planetary system (see Figure 1). This result is expected because the aerodynamic drag on the light particles by the wind is strong, i.e., these particles are more strongly coupled to the gas. For the heavy ($\eta > \eta_t$) particles, on the other hand, drag forces are much less important compared to the gravitational forces from the central star and the disk, and as a result, they fall back into the disk.

3.2. The Effect of Disk Gravity

In this work, we include the gravity of the protoplanetary disk into the calculation of trajectories of solid bodies entrained in X-winds for the first time. Here, we explore the effect of the disk gravity and demonstrate that the disk mass modifies the trajectories and significantly lowers the re-entering radius.

In Figure 2, we plot the trajectories of the same solid body with a different disk mass factor f. If $f = 0$, the disk's gravity is not considered and we return to the situation of Shu et al. (1996). From Figure 2, we find that the disk's gravity has a negligible effect on the trajectory at $l < 1$ AU. Detail analysis on the forces reveals that at $l < 1$ AU, the gravity of the central star provides the major force in the $-\mathbf{e}_z$ direction. When $l > 1$ AU, the trajectories under different f become different. At such a distance, the gravity of the protoplanetary disk becomes comparable with the gravity of the central star in the $-\mathbf{e}_z$ direction. As a result, the solid body flies closer to the disk (smaller z at the same l) when the disk is more massive (larger f). Therefore, the re-entering radius becomes smaller also when the disk is more massive. Comparing the MMSN disk case to the non-disk case, the re-entering radius decreases by $\sim$10%. If we still consider the fact that an actual protoplanetary disk is very likely to be much more massive than the MMSN disk, for example $f = 5$, the re-entering radius can be lowered by up to $\sim$30%.

Here, we find that the protoplanetary disk provides a non-negligible force in the $-\mathbf{e}_z$ direction and modifies the trajectories at $l > 1$ AU. The previous calculations of Shu et al. (1996) that did not consider the disk gravity are therefore imperfect in estimating the re-entering radius.

3.3. The Retention of Solids

In this section, we study the sensitivity of η_t on the disk's mass f and the initial launching angle θ_0. We show how η_t depends on f and θ_0 in Figure 3. By definition, solid bodies of $\eta < \eta_t$ entrained in X-winds are expelled from the solar system. As mentioned in Section 2.2, we consider a solid body to have been

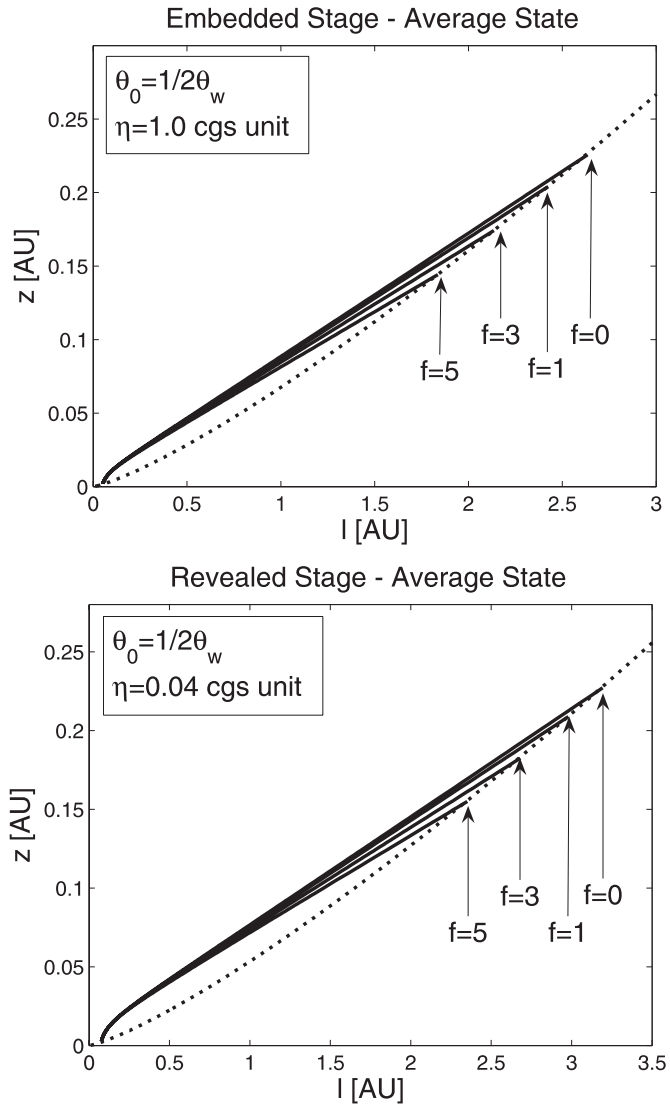

Figure 2. Top: trajectories of a solid body of $\eta = 1.0$ cgs unit entrained in the X-wind in the EA state with $\theta_0 = \theta_w/2$. Bottom: trajectories of a solid body of $\eta = 0.04$ cgs units entrained in the X-wind in the RA state with $\theta_0 = \theta_w/2$. In both panels, the trajectories correspond to the disk mass factor $f = 0$, 1, 3, 5, respectively. The dotted lines show the scale height of the disk. Note that the vertical and horizontal scales in these panels are different.

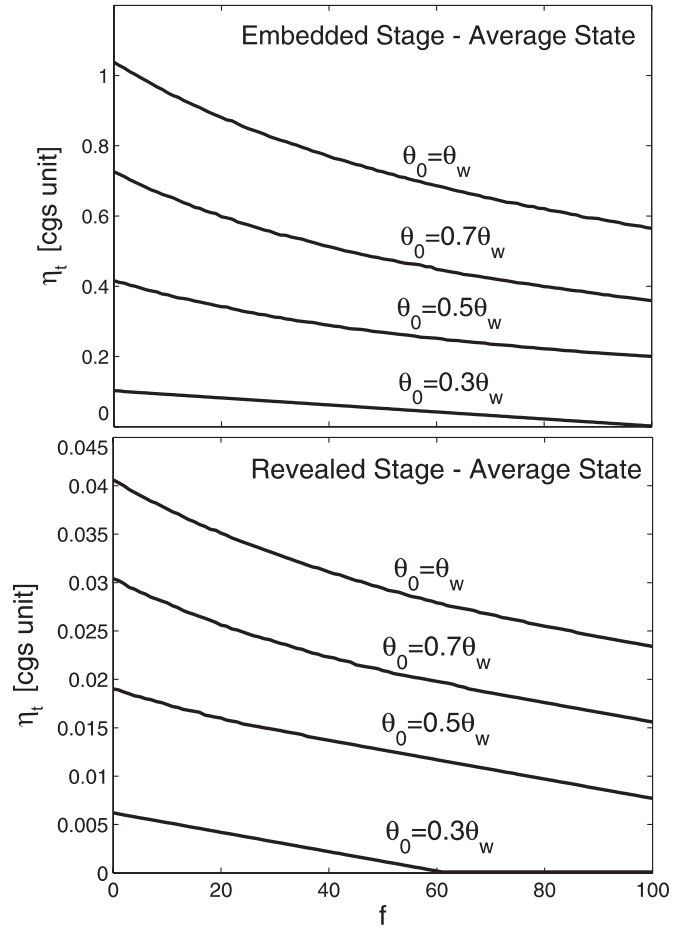

Figure 3. Sensitivity of the threshold η_t on f and θ_0 in the EA (top) and RA states (bottom). For each line, we fix the value of θ_0 as shown in the figure, vary f, and find the corresponding η_t.

expelled if $l > 40$ AU in the trajectory calculation. Note that the value of η_t will change if this cutoff changes.

From Figure 3, the threshold η_t depends most sensitively on the initial launching angle θ_0. Typically, when $f < 10$, η_t at the maximum launching angle $\theta_0 = \theta_w$ is one order of magnitude greater than that at a lower launching angle of $\theta_0 = 0.3\theta_w$. For example, during the EA state and $f = 5$, $\eta_t \sim 0.98$ cgs units at $\theta_0 = \theta_w$; and $\eta_t \sim 0.09$ cgs units at $\theta_0 = 0.3\theta_w$. Similarly, during the RA state and $f = 5$, $\eta_t \sim 0.039$ cgs units at $\theta_0 = \theta_w$; and $\eta_t \sim 0.006$ cgs units at $\theta_0 = 0.3\theta_w$.

When the disk becomes more massive, the solids need to be smaller and lighter in order to be expelled by the X-winds. As seen in Figure 3, η_t decreases by ~10% when f increases from 0 to 10, and η_t decreases by ~30% when f increases from 0 to 100. The dependence of η_t on f is less sensitive, but should also be taken into account when considering the retention of solids in the protoplanetary disk.

The X-wind is stronger during the embedded stage, as a result, η_t during the embedded stage is much larger than that during the revealed stage, as shown in Figure 3. It is interesting to note that η_t during the revealed stage is compatible with the typical chondrule size range in meteorites, if the density is assumed to be 2–4 g cm^{-3}. Finally, an important observation that we can make from Figures 1 and 3 is that the horizontal distance that a solid body can travel depends on its size and density (η) very sensitively.

3.4. The Size-sorting Effect

In this section, we investigate how the re-entering radius depends on the stellar magnetic dipole moment and size and density of the solid bodies. We calculate the trajectories of solid bodies of different η in the states listed in Table 1 and plot the relations between η and the re-entering radius for each state in Figure 4. There are still flexibilities in choosing the value of parameter f and θ_0. In a particular state, a solid body can be launched to the maximum re-entering radius when $f = 0$ and $\theta_0 = \theta_w$, as plotted in Figure 4. There is no theoretical minimum of the re-entering radius for any particular state, since θ_0 can be as low as 0. However, we still plot the re-entering radius with $f = 5$ and $\theta_0 = \theta_w/2$ in Figure 4 to indicate how small the re-entering radius can be for the intermediate lift of any particular state. Again, it is evident that smaller bodies re-enter the disk at larger radii.

The main result that one can draw from Figure 4 is that only the solid bodies whose η are larger than but very close to η_t of a particular state can be launched to the annuli of AB or KB.

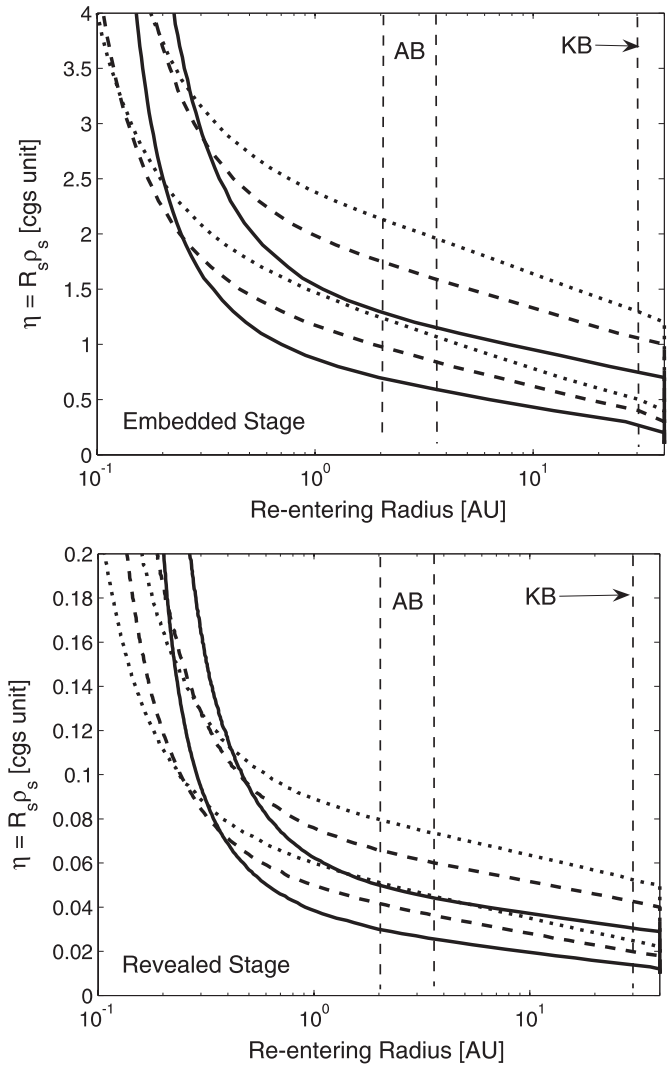

Figure 4. Relations between the solid body size and density (η) and the re-entering radius. Vertical light dashed lines indicate the radii of the AB and the KB of the solar system. For both stages, the solid curves describe the high state, the dashed curves describe the average state, and the dotted curves describe the low state. Each state is described with two curves. The higher curve corresponds to $f = 0$ and $\theta_0 = \theta_w$, and the lower curve corresponds to $f = 5$ and $\theta_0 = \theta_w/2$.

For example, during the EH state and $f = 0$, $\theta_0 = \theta_w$, $\eta_t \sim 0.7$ cgs units, and the solid bodies with $\eta \sim 1.1$–1.3 cgs units re-enter the disk at the AB radius (see the solid curve of the top panel of Figure 4). For another example, during the RH state and $f = 0$, $\theta_0 = \theta_w$, $\eta_t \sim 0.03$ cgs units, and the solid bodies with $\eta \sim 0.04$–0.05 cgs units re-enter the disk at the AB radius (see the solid curve of the bottom panel of Figure 4). The densities of chondrules and CAIs are in a narrow range around 2–4 g cm^{-3} (e.g., Hudges 1980). As a result, η_t is in general equivalent to the threshold size. Of course, meteoritic parent bodies may have a wider feeding zone than the current AB location during their formation. However, the result does not change even if we consider a wider feeding zone, because in order to be lifted to a radius larger than 1 AU, the solid body must already have a size close to the threshold size (see Figure 4).

In any particular state, the location of the AB, where we envisage the parent bodies of carbonaceous chondrites, can only receive solid bodies with sizes larger than but very close to the threshold size. However, the variation of initial launching angle θ_0 affects η_t significantly (see Figure 3) and enlarges the acceptable range of η significantly. In reality, we know very little about the distribution of θ_0. The X-wind model (Shu et al. 2001) suggests that the magnetorotational instability (MRI) occurs at the X-point to transport the rocks from the reconnection ring to the launching height. Based on the turbulent nature of the process, it is reasonable to assume that the distribution of θ_0 is very wide, or nearly uniform. Imagine the CAIs and chondrules form in the X-region and are launched in X-wind from a wide range of θ_0. Due to this variation of θ_0, in any particular state, the annuli of the AB can receive a wide spectrum of solid bodies with different η, in other words, different sizes. For example, during the EH state, if the condition ($f = 0$, $\theta_0 = \theta_w$) is specified, the range for η to re-enter the AB radius is 1.1–1.3 cgs unit (see the solid curves of the top panel of Figure 4). However, once the variation of θ_0 from θ_w to $\theta_w/2$ is considered, the range for η to re-enter the AB radius becomes as wide as 0.6–1.3 cgs unit. In the previous section, we find that η_t depends most sensitively on θ_0, so here the enlargement of the η range is mainly due to the variation in θ_0.

Liffman (2005) predicts very effective size sorting and very sharp size distributions in a constant outflow. This is because in Liffman (2005), the initial launching angle of particles is fixed, corresponding to a single curve in our Figure 4. Here, we step forward to suggest that the variation of θ_0 may make the size distribution of CAIs or chondrules in chondrites wider.

The second result is that an annulus of the protoplanetary disk receives one order of magnitude smaller solid bodies (assuming the density is generally the same) during the revealed stage than during the embedded stage. For example the location of AB receives solid bodies of $\eta \sim 0.8$–1.7 cgs units during the EA state, but solid bodies of $\eta \sim 0.04$–0.07 cgs units during the RA state, with the uncertainty of f and θ_0 ($\sim [\theta_w/2, \theta_w]$) considered. Table 1 shows that only the EA and EL states can reach the required temperature $T_{\rm peak} > 1800$ K and produce CAIs. In contrary, chondrules need lower temperature and are younger than CAIs (e.g., Scott 2007). It is then likely that chondrules mainly formed during the revealed stage. If this is the case, the chondrules should be smaller than CAIs in any particular chondritic group because of the X-wind transport. However, such difference could not be found in chondrites (e.g., Scott 2007). We will address this discrepancy in the following section.

Last but not the least, the variations of re-entering radius according to μ_* are different for small and large bodies. As the star becomes less magnetized, the small solid body re-enters the disk at a larger radius, but the large solid body re-enters the disk at a smaller radius. This feature may counter the physical intuition. Actually, as μ_* decreases, or the star becomes less magnetized, the accretion disk is truncated at a smaller radius. However, the star rotates much faster according to Equation (2) so that the terminal velocity of the X-wind becomes faster. For small bodies, the wind terminal velocity determines how much momentum it can gain during the aerodynamic launching phase; therefore, a less magnetized star produces faster winds, and then solid bodies re-enter the disk at larger radii. For large bodies, their aerodynamic launching phase is very short and their re-entering radii are close to the truncation radius $R_{\rm X}$.

4. DISCUSSION

In any particular state of X-winds, f, θ_0, and η determine whether an entrained solid body re-enters the disk, as well as the re-entering radius. Section 3.3 shows that the retention of

solid bodies depends most sensitively on the initial launching angle θ_0. Especially, small bodies fall back to the disk if they are launched at a sufficiently small launching angle. In order to estimate the percentage of entrained solid bodies that eventually fall back, one has to know the distribution of θ_0, which relates to complicated processes of retrieving materials from the reconnection ring.

Although blurred by the uncertainty in θ_0, the size sorting effect of X-winds may have significant implications in our understanding of CAI and chondrule populations. Because of the uncertainty in θ_0, the present model can only provide an upper limit of η below which a solid body can be delivered by X-winds to a certain location of the disk.

Based on Figure 4, the acceptable η for a solid body to be delivered to the location of the AB during the revealed stage is up to 0.08 cgs units. If we assume chondrules mainly formed during the revealed stage and the density of chondrules is in the range of 2–4 g cm^{-3} (e.g., Hudges 1980), the X-wind transport model here predicts the maximum chondrule radius to be ∼0.04 cm, compatible with all carbonaceous chondrite groups except the CV class (e.g., Wurm & Krauss 2006). In average, CV chondrites have largest chondrules with size of ∼0.1 cm. From Figure 4, chondrules in CV chondrites cannot be delivered to the location of the AB during the revealed stage. Instead, they might form during the EH state, or during the transitional stage between the embedded stage and the revealed stage.

In particular, CH chondrites have the smallest chondrules with a size of ∼0.002 cm (Jones et al. 2000). According to our X-wind transport model, a solid body as small as the chondrules in CH chondrites can easily be expelled from the system. One possible way to retain such tiny objects is to have a very small initial launching angle θ_0. However, if the chondrules that formed in the X-region were launched isotropically at all angles in $[0,\ \theta_w]$, large ones should be delivered simultaneously to the location of the AB. Therefore, chondrules need to be launched preferably at small launching angles in order to explain the depletion of large chondrules in CH chondrites. Another possible explanation is that the chondrules of CH chondrites were delivered at the very end of the revealed stage, when the disk accretion and the X-wind approached the end. If this is the case, chondrules in CH chondrite experienced the thermal treatment of a lower temperature, which could be tested by mineralogical examinations.

CAI-type and chondrule-like particles found in a short-term comet 81P/Wild 2 are very small having a size of ∼20 μm (e.g., Brownlee et al. 2006; Nakamura et al. 2008). X-winds could easily expel these tiny objects from the solar system (see Figure 4). However, the particles had been larger than their present size because they were ablated and disaggregated during the deceleration in the aerogel (Flynn et al. 2006). The entrance-hole sizes of impact tracks place an upper limit for the size of the initial incoming particles, which is about 0.1 cm (or $\eta \sim 0.3$ cgs unit). From Figure 4, the solid bodies with such sizes can be transported to the KB during the embedded stages.

CAI sizes are also different in various chondritic groups (Hezel et al. 2008), correlating with the chondrule sizes. CV chondrites appear to have the largest CAIs with size range in 0.01–0.15 cm, and CH chondrites have the smallest CAIs with size generally <0.01 cm (e.g., Zhang & Hsu 2009). Because CAI formation requires high temperature, only the EA and EL states are suitable (see dotted and dashed curve in the top panel of Figure 4). We find that CAIs in all chondritic groups are lighter than the threshold η_t of $\theta_0 = \theta_w/2$ during the EA and EL states. Therefore, for these tiny primitive grains to be retained in the disk, the current X-wind model requires that they are launched preferably at low initial launching angles ($\theta_0 < \theta_w/2$). This requirement provides a new aspect to test the X-wind model, and also suggests the importance of understanding the initial θ_0 distribution.

Finally, according to Figure 4, large solid bodies whose η well exceeds η_t cannot be lifted over long distances. They will re-enter the inner disk and follow the accreting inflow. It is possible that they enter the reconnection ring for the second time, during the timescale of the embedded or revealed stage. After being thermally processed for the second time, they are expelled again by X-winds and then may enter a larger orbit if they experience some fragmentation. Especially, independent enveloping compound chondrules have a secondary layer of chondrule-like material enclosing an unrelated primary, indicating that they experience multiple melting (Wasson et al. 1995). It would be very interesting to study the role of X-winds in the multiple thermal treatments of such chondrules.

5. CONCLUSION

In this work, we calculate the trajectories of solid bodies entrained in X-winds with the consideration of the protoplanetary disk's gravity and geometry. We find that the disk's gravity becomes comparable to the gravity of the central star at $l > 1$ AU, and the disk's mass affects the trajectories and the location where the solid bodies re-enter the disk significantly. The gravity of a disk whose mass is five times of the MMSN disk can lower the re-entering radius by up to 30%.

The product of the size and the density, denoted as η in this paper, is the key parameter in evaluating the efficiency the gas drag and the sorting effect. We find a threshold value of η, denoted as η_t, for any particular X-wind state, disk's mass, and initial launching angle. Solid bodies with $\eta < \eta_t$ are expelled by the X-wind from the solar system. We find that η_t depends most sensitively not only on the initial launching angle θ_0, but also on the disk's mass factor f.

We demonstrate again the size-sorting effect of the X-wind transport by showing that only the solid bodies with an η larger than but very close to η_t can be launched to the location of the AB. We also find that the variation of the initial launching angle may smooth out the size-sorting effect, because solid bodies with a wider range of η can be delivered to the desired location. This improved X-wind transport model is consistent with the chondrule size in all carbonaceous chondrite groups other than CV and CH. The size of chondrules in CV and CH chondrites, as well as the size of CAIs in carbonaceous chondrites, requires additional mechanisms to be explained.

In order to compare the model prediction with the measured chondrule size distribution, it is necessary to further calculate the η distribution after the X-wind size sorting. To do so, one has to know the initial size distribution as well as the distribution over the initial launching angle, which are determined by the formation mechanism of chondrules in the X-region. Furthermore, there is little constraint on the variation of the stellar magnetic dipole moment. The final η distribution reflects the entire evolution history of the early Sun. For example, if the stellar activity remains stable for a long period of time, we should see relatively sharp size distributions of chondrules. Therefore, the η distribution of chondrules may contain valuable information of the early solar system.

R.H. is grateful to S. Seager for helpful advice in the preparation of the manuscript, L. Elkins-Tanton for the encouragement of publication of this work, J. Meyer and B. Weiss for helpful discussions, and the anonymous referee for the improvement of the manuscript.

REFERENCES

Brownlee, D., et al. 2006, Science, 314, 1711
Ciesla, F. J. 2009, Icarus, 200, 655
Clayton, R. N. 1993, Annu. Rev. Earth Planet. Sci., 21, 115
Clayton, R. N. 2002, Nature, 415, 860
Desch, S. J. 2007, ApJ, 671, 878
Desch, S. J., Morris, M. A., & Connolly, H. C. 2010, Lunar and Planetary Science Conf. Abstracts, 41, 2200
Flynn, G. J., et al. 2006, Science, 314, 1731
Hartmann, L. 2009, Accretion Processes in Star Formation (2nd ed.; Cambridge: Cambridge Univ. Press)
Hayashi, C. 1981, Prog. Theor. Phys. Suppl., 70, 35
Hezel, D. C., Russel, S. S., Ross, A. J., & Kearsley, A. T. 2008, Meteorit. Planet. Sci., 43, 1879
Hudges, D. W. 1980, Earth Planet. Sci. Lett., 51, 26
Jones, R. H., Lee, T., Connolly, H. C., Love, S. G., & Shang, H. 2000, in Protostars and Planets IV, Formation of Chondrules and CAIs: Theory vs. Observation, ed. V. Mannings, A. P. Boss, & S. S. Russell (Tucson, AZ: Univ. Arizona Press), 927
Liffman, K. 2005, Meteorit. Planet. Sci., 40, 123
Nakamura, T., et al. 2008, Science, 321, 1664
Rubin, A. E. 2000, Earth Sci. Rev., 50, 3
Scott, E. R. D. 2007, Annu. Rev. Earth Planet. Sci., 35, 577
Shang, H. 1998, PhD thesis, Univ. of California, Berkeley
Shu, F. H., Najita, J., Ostriker, E., Wilkin, F., Ruden, S., & Lizano, S. 1994a, ApJ, 429, 781
Shu, F. H., Najita, J., Ruden, S., & Lizano, S. 1994b, ApJ, 429, 797
Shu, F. H., Shang, H., Glassgold, A. E., & Lee, T. 1997, Science, 277, 1475
Shu, F. H., Shang, H., Gounelle, M., Glassgold, A. E., & Lee, T. 2001, ApJ, 548, 1029
Shu, F. H., Shang, H., & Lee, T. 1996, Science, 271, 1545
Swindle, T. D., & Campins, H. 2004, Meteorit. Planet. Sci., 39, 1733
Tayler, S. R. 1992, Solar System Evolution (Cambridge: Cambridge Univ. Press)
Wasson, J. T., Krot, A. N., Lee, M. S., & Rubin, A. E. 1995, Geochim. Cosmochim. Acta, 59, 1847
Weidenschilling, S. J. 1977, MNRAS, 180, 57
Wooden, D. H. 2008, Space Sci. Rev., 138, 75
Wurm, G., & Krauss, O. 2006, Icarus, 180, 487
Youdin, A. N., & Chiang, E. I. 2004, ApJ, 601, 1109
Zhang, A., & Hsu, W. 2009, Meteorit. Planet. Sci., 44, 787